High Temperature Strategy for Oxide Nanoparticle Synthesis

Geneviève Mialon, Morgan Gohin, Thierry Gacoin, and Jean-Pierre Boilot*

Groupe de Chimie du Solide, Laboratoire de Physique de la Matière Condensée, CNRS, École Polytechnique, 91128 Palaiseau cedex, France

ABSTRACT Compared with noble metals and quantum dots, dielectric complex oxide nanoparticles are significantly less popular due to their high crystallization temperature, making difficult their synthesis in the 10—100 nm range for which surface effects are reduced. We report here an original process permitting thermal annealing of complex oxide nanoparticles at high temperature without aggregation and growth. Thus, after thermal treatment, these annealed particles can be dispersed in water, leading to concentrated aqueous colloidal dispersions containing isolated highly crystalline particles. This contrasts with usual colloidal techniques for which the production of particles in the 10—100 nm range generally leads to poorly crystallized particles, especially for multicomponent oxides. From two examples, we show some possibilities offered by this type of process. This concerns the synthesis of lanthanide-doped oxide nanoparticles exhibiting a bulk behavior for their luminescence properties and the control of the composition in nitrogen-doped titanium oxide particles without sintering and size change.

KEYWORDS: oxide nanoparticles · colloidal synthesis · luminescent nanoparticles · photocatalysis · mesoporous silica

Colloidal syntheses to prepare size-controlled and monodisperse nanocrystals have been largely developed in the last years, especially for semiconducting quantum dots and metals. Dielectric oxides constitute an important other class of nanoparticles used as colloids in different types of applications. For example, oxide nanoparticles (ONPs) in colloidal suspensions are of great interest for biomedical and environmental research applications:

Magnetic ONPs (especially maghemite γ-Fe_2O_3) have been used in various biomedical applications, such as drug delivery, magnetic resonance imaging, and hyperthermia cancer treatment.[1−3]

Luminescent lanthanide-doped ONPs (such as doped oxides Y_2O_3, vanadates YVO_4, and phosphates $LaPO_4$) have been proposed as a new class of biological fluorescent probes that are promising for single-molecule tracking applications.[4−6]

Semiconducting ONPs (TiO_2, ZnO) have raised extensive interest for photocatalytic applications in which organic molecules are photodegraded, such as water and air purification and self-cleaning coatings.[7−9]

ONPs were generally prepared as nanocrystals in the 1−10 nm range from liquid-phase syntheses in water (hydrothermal synthesis) or in high-boiling-point coordinating solvents.[10,11] However, contrasting with noble metals and semiconductor for which nanocrystals display properties found to be scientifically different from the bulk material, yielding rich and application-oriented research,[12] dielectric ONPs only exhibit less efficient properties due to surface effects or structural defects. As examples, compared with corresponding bulks, the yield of luminescent ONPS is decreased by nonradiative surface recombination processes[13−15] and the magnetization of magnetic ONPs is decreased due to lower effective magnetic interactions caused by surface termination.[16] A first condition to obtain ONPs with the bulk behavior is obviously to synthesize particles in the 10−100 nm size range where the number of atoms at the surface is largely decreased (less than 10% above 10 nm), limiting surface effects. However, the degradation of oxide properties is generally amplified in this size range as the particles prepared from liquid-phase syntheses are poorly crystallized, consisting in aggregates of smaller units. Moreover, in contrast with the huge variety of bulk oxide compounds, only a very small number of compositions are known for ONPs dispersed in a colloidal state. The reason is that the preparation of well-crystallized complex oxides generally requires high temperature treatment (typically above 1000 °C), leading to irreversible growth and coalescence of starting particles resulting from mass movements associated to diffusion mechanisms.

*Address correspondence to jean-pierre.boilot@polytechnique.edu.

Received for review September 15, 2008 and accepted October 30, 2008.

Published online November 12, 2008.
10.1021/nn8005784 CCC: $40.75

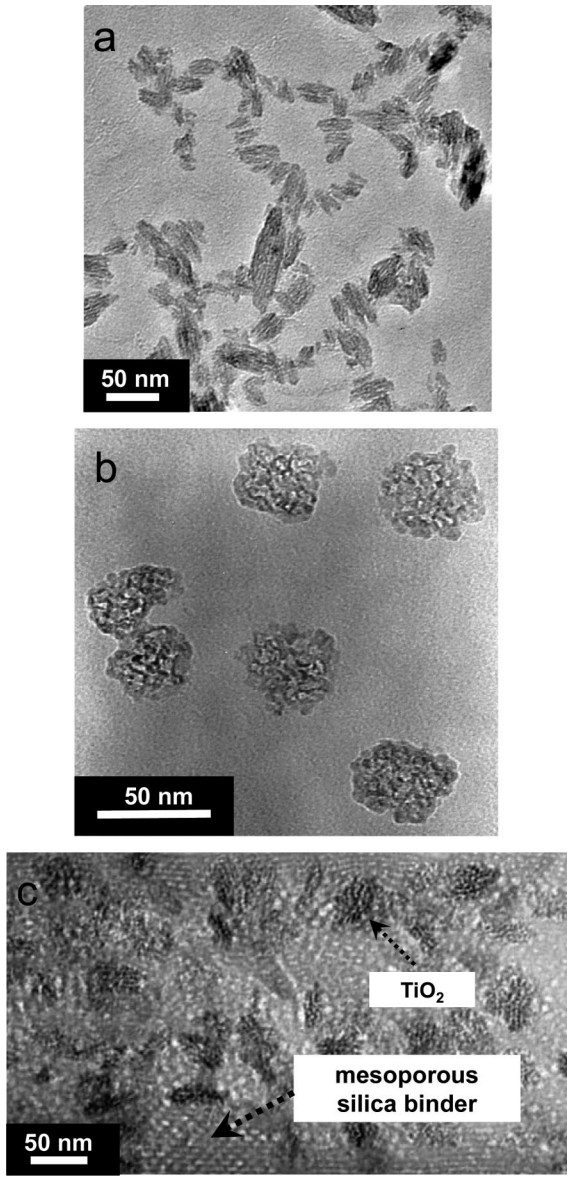

Figure 1. TEM images of crude NPs and of silica/NPs composites. (a) Colloidal YVO_4:Eu (10% Eu^{3+}) NPs and (b) colloidal TiO_2 NPs deposited on a thin carbon grid. (c) TiO_2 NPs dispersed in a mesoporous silica matrix (Ti/Si = 0.25) obtained with a copolymer template and heating at 450 °C to remove the organic groups.

Here we report an original process permitting thermal annealing of ONPs at high temperature (up to 1000 °C) without a significant growth and without particles adhering to each other. In comparison with usual techniques of preparation of ONPs performed at low temperature (from room temperature to 300 °C), this high temperature technique is able to produce perfectly crystallized particles in the 10−100 nm range. Moreover, after thermal treatment, the process allows dispersing annealed particles in water, leading to concentrated aqueous colloidal dispersions of multicomponent oxides containing isolated highly crystalline particles.

The process can be broken down into the following steps: a concentrated aqueous dispersion of crude oxide nanoparticles was early prepared using colloidal techniques such as a precipitation reaction at room temperature. Using the well-known sol−gel technique, crude nanoparticles were then mixed in a silica sol using a copolymer both as a dispersing agent to prevent particle aggregation and as a structure directing agent to obtain a mesostructured silica network. After silica gelation and copolymer calcination, this leads to homogeneous concentrated dispersion of the crude particles in a highly porous silica matrix (porous volume fraction up to 40%) which ensures the role of a refractory solid dispersing agent. In fact, for oxide particles studied below, no significant interaction was detected between the silica matrix and the starting nanoparticles after thermal treatments up to 1000 °C. Besides, in the presence of nanoparticles and after the thermal treatment, the porous silica matrix was still amorphous and was not significantly sintered, making possible its chemical dissolution without significant alteration of ONPs. Finally, the annealed nanoparticles were purified and dispersed in water by sonification using a stabilizing agent. Structural characterizations from XRD and TEM experiments clearly show that the thermal annealing turns polycrystalline and highly constrains crude units into perfectly crystallized nanoparticles without structural transition, coalescence, and significant size increase.

From two types of particles, YVO_4:Eu and TiO_2, we show here some possibilities offered by this type of process which should be generalized in the near future to prepare highly crystalline ONPs. The first example concerns the large improvement of optical properties for YVO_4:Eu nanoparticles. Especially, in comparison with crude particles, a large increase of the luminescence quantum yield is observed after the annealing, due to the reduction of the Eu^{3+} quenching surface effects. Moreover, in these well-crystallized particles, the luminescence mechanism is dominated by energy transfers as it is known in the bulk.[17,18] Apart from the interest to obtain oxide nanoparticles with the bulk behavior, the new process can also permit the synthesis of nitrogen-doped nanoparticles without sintering and size change. The related example concerns the formation of nitrogen-doped TiO_2 nanoparticles by thermal treatment under ammonia atmosphere, leading to a large doping range into the anatase TiO_2 phase.

RESULTS AND DISCUSSION

YVO_4:Eu crude particles were prepared through a simple precipitation from precursor salts in aqueous solution (see Experimental Section). The process and the structural characterization of the particles were described extensively in our previous paper.[19] As shown in Figure 1a, the initial colloidal suspension consists of dispersed polycrystalline particles exhibiting a prolate ellipsoid shape. Their size follows a log-normal distribution with average axial dimensions of 20 nm (σ = 7 nm) and 39 nm (σ = 16 nm). TiO_2 nanoparticles used

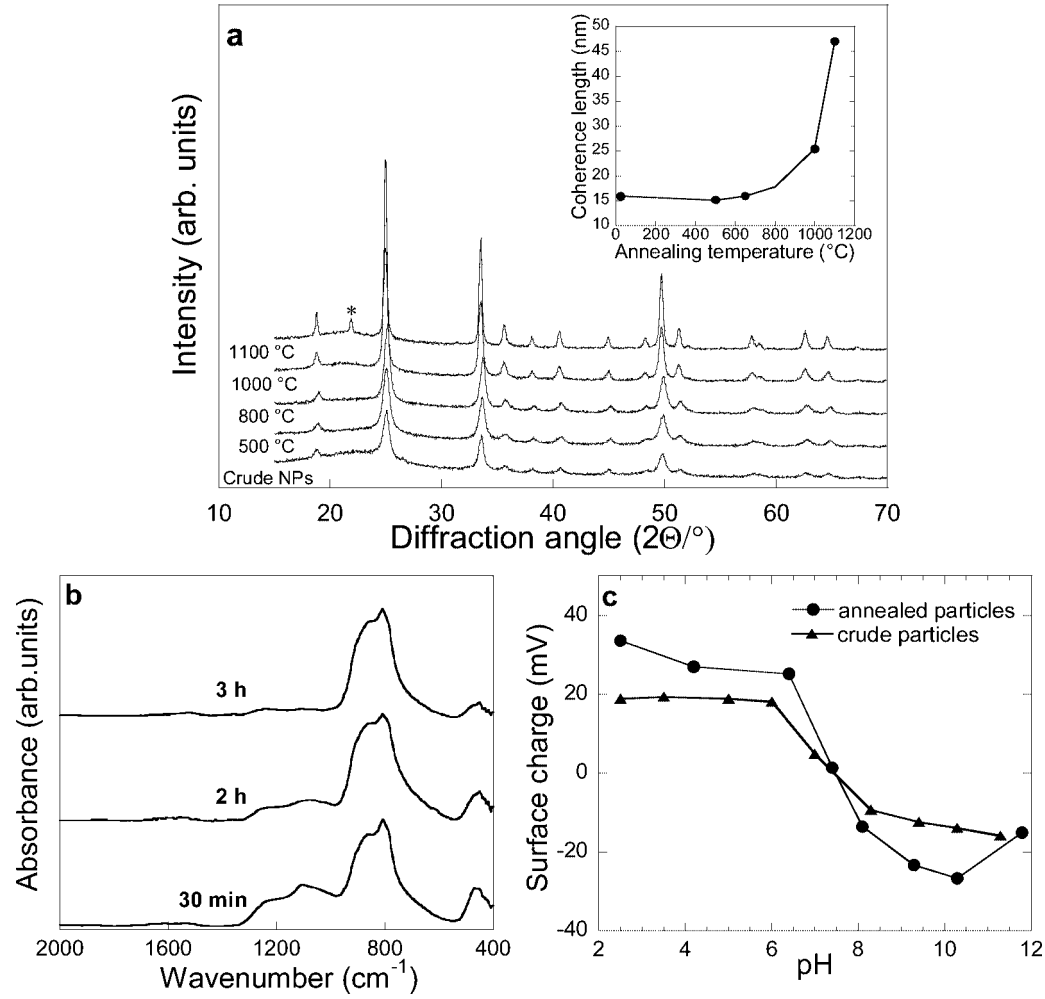

Figure 2. Annealing of ONPs/mesoporous silica composites and recovering of annealed NPs. (a) X-ray diffraction diagrams (Cu Kα) and evolution of the coherence length (inset) as a function of the annealing temperature for silica/YVO_4:Eu (10% Eu^{3+}) NP composites. Peaks correspond to the zircon-type structure. The broad band around Θ = 25° is due to the silica amorphous structure. *SiO_2 cristobalite phase observed at 1100 °C. (b) Hydrofluoric acid attack of silica/YVO_4:Eu NPs composites. As time increases, the intensity of the silica IR band around 1100 cm^{-1} progressively decreases, showing the silica dissolution. The intensity of the vanadate IR band around 800 cm^{-1} is constant, indicating the integrity of YVO_4:Eu NPs. (c) The pH dependence of the surface charge for annealed (1000 °C) and crude YVO_4:Eu NPs in aqueous suspensions. The isoelectric point (pH = 7.2) remains the same after annealing and hydrofluoric acid treatment, suggesting no residual silica around YVO_4:Eu NPs.

in this work are commercially available from Millennium (reference S5-300) as aqueous acidic suspensions (pH = 1 HNO_3). The morphology of the particles is shown in Figure 1b. Their average size is about 50 nm. They are made up of isotropic aggregates of primary particles with an average size of *ca.* 7 nm. Due to their aggregated structure, these particles are porous with a pore volume fraction of 28%.[20]

The synthesis process of the mesoporous silica matrix was directly adapted from our previous work on the elaboration of mesoporous silica films using a polyethylene oxide/polypropylene oxide triblock copolymer (PE6800 $EO_{73}PO_{28}EO_{73}$) as the surfactant.[21] For a copolymer/Si ratio of 0.01 in the initial sol, mesoporous silica materials exhibit a total pore volume fraction of about 38%, distributed both as micropores (*i.e.*, pores with diameter of a few Å) and mesopores (size of 5 to 6 nm) that are arranged with a textured face centered orthorhombic structure. Incorporation of crude nanoparticles into the mesoporous silica matrix was achieved by the simple addition of colloidal dispersions into the acidic silica sol containing the copolymer surfactant (see Experimental Section). For example, the good dispersion state of the TiO_2 particles is preserved for Ti/Si molar ratios up to 4. Rapid flocculation was, however, observed when the particles were added to the sol without the surfactant, and this even for a low Ti/Si ratio. This shows that the copolymer ensures a steric stabilization of the particles through its electrostatic interactions with their surface. After silica gelation and drying, the resulting powder is heated under air to remove organic entities and obtain a mesoporous composite structure. Figure 1c shows a TEM picture of a representative material heated at 450 °C in which the TiO_2 particles are well dispersed in the organized porous structure, as previously observed in pure silica

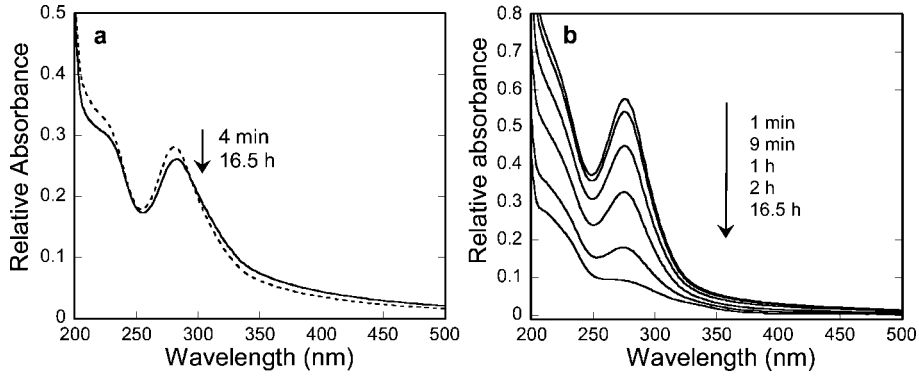

Figure 3. Chemical stability of YVO_4:Eu ONPs. Kinetics of the particle dissolution by HCl solution (0.02 M), deduced from the time evolution of the UV absorbance of vanadate groups, for annealed at 1000 °C (a) and crude (b) particles. The slower acid attack observed for annealed ONPs indicates higher chemical stability for these particles.

films. The mesoporous composite exhibits a total pore volume fraction of about 41%, a surface area of 450 $m^2 \cdot g^{-1}$ and a mesopore size of 4 nm (see Figure 1S in Supporting Information).

After heating in air up to 1000 °C, a first observation concerns the silica matrix which remains amorphous, and porous (surface area of 413 and 75 $m^2 \cdot g^{-1}$ after heating at 800 and 1000 °C, respectively). This contrasts with the behavior observed for pure silica mesoporous samples which appear as sintered (surface area of 2.5 $m^2 \cdot g^{-1}$) and crystallized (cristobalite-type structure) after heating at 1000 °C. This indicates that ONPs act as fillers to slow down the shrinkage of the silica mesoporous structure, avoiding collapse and crystallization of the silica structure up to 1000 °C. Another crucial point is that XRD patterns present the same diffraction peaks before and after heating at 1000 °C (Figure 2a). This means both that there is no significant chemical interaction between TiO_2 or YVO_4:Eu NPs and the porous silica matrix which would lead to the formation of a new phase and that the structural type observed for crude NPs is not changed (zircon for YVO_4:Eu and anatase for TiO_2). However, the peak broadening is significantly reduced as the annealing temperature increases. By fitting various diffraction peaks to the Scherrer formula[22] and taking into account the instrumental broadening, the average coherence lengths increase from 19 ± 6 to 34 ± 5 nm and from 7 ± 2 to 30 ± 3 nm for YVO_4:Eu and TiO_2 NPs, respectively (Figure 2a, inset). Moreover, Williamson and Hall analysis[23] (see Figure 2S in Supporting Information) clearly indicates an important decrease of constraints in annealed NPs suggesting that the increase of the coherence length is due to an improvement of the crystallinity of NPs rather than to their growth. In comparison, the same thermal treatment performed on crude NPS (without the porous silica matrix) induces a growth of particles with a coherence length above 100 nm for the two types of particles, leading to the expected structural transition (anatase to rutile) for TiO_2 NPs. This clearly proves the ability of the porous silica to limit the growth of NPs and to preserve the structural type during their annealing.

The next step of the process consists of the dissolution of the silica matrix and the dispersion in water (see Experimental Section). Concerning the SiO_2/YVO_4:Eu NPs composite, the silica dissolution was performed by hydrofluoric acid 2% in excess[24] (Si:HF molar ratio of 1:9) following the reaction: $SiO_2 + 6HF \rightarrow H_2SiF_6 + 2H_2O$. Basic dissolutions with tetramethylammonnium or potassium hydroxides are other possible routes. As the orthovanadate and silica bands on FTIR spectra are well-defined and specific around 00 and 1100 cm^{-1}, respectively (see Figure 2b), peak integration and calibration curves allow estimating the amount of remaining silica around NPs and consequently determining the optimum time for complete silica dissolution. After purification by centrifugation to eliminate hydrofluoric acid in excess and dissolved silica, the NP powder was diluted in water. Zeta-potential analysis indicates that the isoelectric point is at pH = 7.2 for annealed and crude NPs (see Figure 2c), while the one of silica is around pH = 2.[25] This confirms both the absence of a silica shell around the particles, in agreement with chemical analysis, and that the surface state of particles is not drastically modified by the annealing. The final NP aqueous suspension was stabilized at pH = 10 by adding poly(acrylic acid) (V:PAA 1:0.05) and sonicated in a cold bath. A similar strategy was used for SiO_2/TiO_2 NP composites, but the annealed NP aqueous suspension was stabilized at pH = 1 by adding HNO_3.

The integrity of the YVO_4:Eu phase during the annealing is verified by recording the time evolution of the UV band characteristics of the orthovanadate groups at 275 nm. For NPs annealed at 1000 °C, the intensity of this band is only slightly changed after that all the complete dissolution of the silica is performed. This shows that the kinetics is largely slower for the dissolution of the vanadate compared with silica one in these annealed NPs. Moreover and as expected, it is clearly observed that the well-crystallized annealed NPs present higher chemical stability compared to crude ones for which an acid attack (HCl 0.02 M) was much faster (see Figure 3a,b).

Figure 4a presents an electron microscopy photograph performed on isolated $Y_{0.9}Eu_{0.1}VO_4$ NPs after annealing. The initial ellipsoidal form of particles is less marked after annealing at 1000 °C with the formation of plain facets and different shapes (square, rectangular, or pentagonal). Note that the annealing does not induce a significant increase of size (see Figure 4b,c), con-

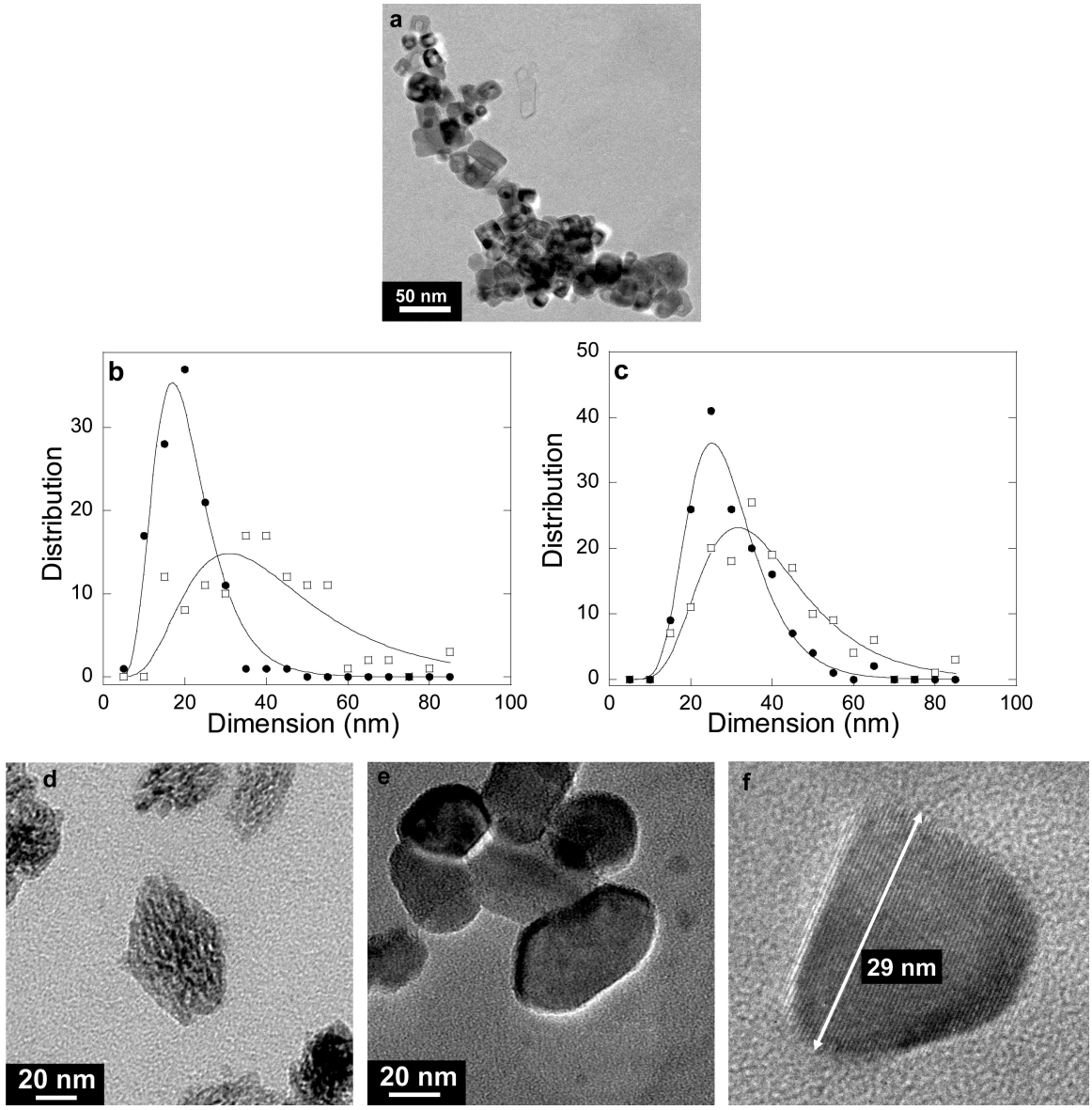

Figure 4. Shape, size, and structure of annealed YVO_4:Eu NPs. (a) TEM image of YVO_4:Eu (10% Eu^{3+}) NPs after annealing at 1000 °C (b,c) Size distribution curves (black and white squares correspond to length and width particle measurements, respectively), deduced from TEM and SEM images, assuming a prolate ellipsoid shape and a log-normal size distribution. Average axial dimensions are 20 nm (σ = 7 nm) and 39 nm (σ = 16 nm) for crude NPs and 29 nm (σ = 9 nm) and 39 nm (σ = 15 nm) after annealing at 1000 °C. (d,e) TEM images after annealing at 800 and 1000 °C, respectively. (f) TEM image showing reticular planes for an isolated particle annealed at 1000 °C.

firming that the porous silica matrix well prevents the growth of NPs. Moreover, while NPs still appear as polycrystalline on TEM photographs after annealing at 800 °C, improvement of the contrast and change of the morphology after annealing at 1000 °C suggest an evolution to single crystalline NPs due to a self-sintering process (see Figure 4d,e). This is confirmed by the similarity between the average size of annealed NPs and their coherence length value deduced from XRD patterns. Note that this sharp evolution of the structure after annealing in the 800−1000 °C range leads to ONPs with a perfect crystallized state (see Figure 4f), which is obviously not reached from a liquid-phase synthesis.

A first expected interest for this process concerns the impact on the physical properties of ONPs. As previously discussed, the red luminescence properties of YVO_4:Eu compounds are governed by energy transfers occurring after the absorption of light, taking place through exchange (VO_4−Eu),[17] and multipolar (Eu−Eu) interactions.[18] These transfers are all the more favored when the wave function overlaps are efficient as in the bulk material, making them highly sensible to structural defects. Figure 5 shows the evolution of the emission quantum yield for $Y_{1-x}Eu_xVO_4$ suspensions, under excitation at 280 nm in the orthovanadate band, as a function of the Eu concentration before and after annealing at 1000 °C. In comparison with crude particles, the

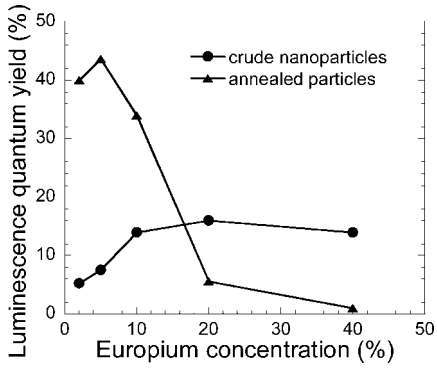

Figure 5. Luminescence properties of annealed YVO_4:Eu NPs. Evolution of the luminescence quantum yield as a function of the europium content for crude and annealed NPs at 1000 °C.

quantum yield is largely increased in annealed particles (37% instead of 14% for 10% Eu), and the quantum yield of annealed NPs is not significantly changed when the colloidal solution is transferred into deuterated water. This contrasts with the behavior of crude particles for which previous studies have shown that surface OH groups are efficient quenchers of the excited europium ions.[19,26] The reduction of surface quenching effects in annealed NPs is probably related to the structural reconstruction of NPs at high temperature by the self-sintering process, which decreases the OH adsorption. In fact, the surface area of a powder of annealed particles is only of 10 $m^2 \cdot g^{-1}$, instead of 200 $m^2 \cdot g^{-1}$ for crude NPs. This shows a significant decrease of the porosity and of the surface roughness of NPs, leading therefore to a reduction of the number of accessible Eu ions for the adsorption of OH groups.

In addition, while no well-defined maximum is observed on the curve showing the europium concentration dependence of the luminescence yield for crude nanoparticles, it can be noted that the annealed NPS present, as for the bulk material, an optimum of the europium concentration around 5%.[27] This comes from two competitive effects: on the one hand, an increase of the europium concentration improves the probability of the VO_4−Eu energy transfers and thus radiative recombination. However, on the other hand, the increase of the probability of Eu−Eu energy transfers increases the efficiency of the excitation capture by nonradiative recombination centers. All these results clearly demonstrate that the energy transfer efficiency is high for annealed well-crystallized NPs, similarly to bulk materials. Therefore, the annealing process furnishes highly bright nanophosphors which are potential candidates as biological luminescent labels or for integration in transparent luminescent coatings. More generally, this process appears able to produce ONPs exhibiting similar physical properties that corresponding bulk materials.

Another potentiality of the annealing process concerns the control of the chemical composition in ONPs and is now illustrated from the annealing of TiO_2 anatase NPs. In the photocatalysis field, most of the investigations have focused on titanium dioxide (TiO_2) which shows relatively high reactivity under UV light, whose energy exceeds the band gap of 3.2 eV in the anatase crystalline phase. Intense research has been recently devoted to the preparation and characterization of nitrogen-doped titanium dioxide ($TiO_{2-x}N_y$) materials to produce an active photocatalyst under visible light, so that sunlight can be more efficiently used in photocatalysis.[28,29] To incorporate nitrogen in the anatase structure, different strategies have been used that all lead to thin films or bulk materials containing agglomerated particles. The synthesis of isolated N-doped TiO_2 NPs with high surface area could be a promising way to exalt the photocatalytic activity as previously shown for pure TiO_2 particles dispersed in porous silica films.[30]

Using the original annealing treatment of NPs in the NH_3 atmosphere, we have prepared colloidal suspensions of $TiO_{2-x}N_x$ nanoparticles. After heating the SiO_2/TiO_2 NP composite for 2 h at 700 °C in ammonia atmosphere, the powder is brown. Porous silica and anatase NPs were detected on X-ray patterns (see Figure 6a). To investigate N states in $TiO_{2-x}N_y$, N 1s core levels were measured with X-ray photoemission spectroscopy (XPS). The atomic β-N peaking at the binding energy of 396 eV was used to quantify the N concentration in annealing NPs. When increasing heating temperature in air from 300 to 500 °C, the powder becomes brown (N/Ti = 6%), yellow (N/Ti = 3%), and white (N/Ti

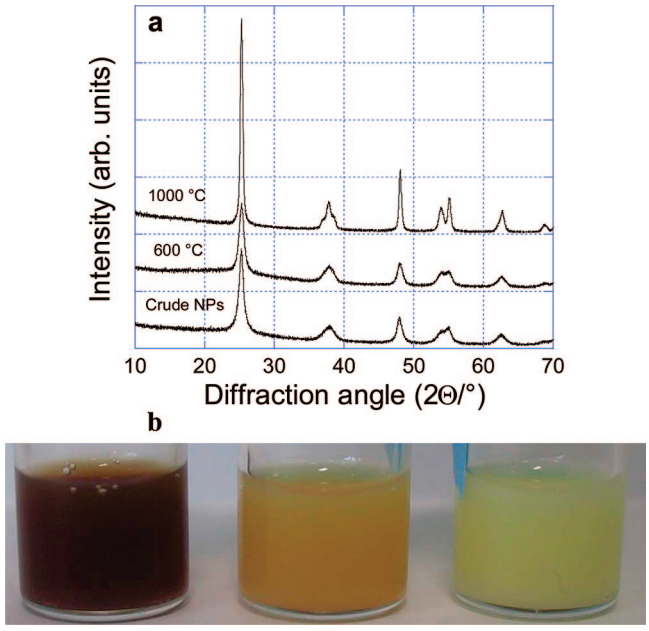

Figure 6. Structure and colloidal suspensions of N-doped TiO_2 NPs. (a) X-ray diffraction diagrams (Cu Kα) as a function of the annealing temperature for TiO_2 NPs. Peaks correspond to the anatase type structure. (b) Photographs of aqueous suspensions containing N-doped TiO_2 NPs annealed 2 h at 700 °C under NH_3 (left), then heated 2 h in air at 300 °C (left), at 400 °C (middle), or 500 °C (right).

$< 1\%$), corresponding to a progressive decrease of the N concentration in NPs. After dissolution of the porous silica, purification, and dispersion of particles in an acidic medium, a wide range of colloidal aqueous suspensions of $TiO_{2-x}N_x$ anatase NPs were prepared (Figure 6b), presenting active wavelength less than 500 nm, making them promising for different applications such as water purification.[31]

CONCLUSION

We have developed a simple method to prepare well-crystallized ONPs in the 10−100 nm size range and also demonstrated an interest to prepare pure ONPs and N-doped ONPs with bulk properties. In the near future, this process should allow preparing a large variety of multicomponent oxides which are not known in the ONPs field and also to observe new physical properties for ONPs. As an example, a clear challenge for the chemist is to shift excitation wavelength of luminescent NPs toward the infrared range. This could be obtained by developing new oxide nanoparticles able to emit visible light by the up-conversion process.[32,33] However, up to now, no aqueous phase synthesis has led to efficient ONPs due to surface quenching effects. Using our original annealing process, we have, for the first time, succeeded in observing the up-conversion luminescence of Yb,Er-doped YVO_4 NPs in water with a strong green emission for an excitation at 980 nm.

EXPERIMENTAL SECTION

Synthesis of YVO_4 Nanoparticles. An aqueous solution of yttrium nitrate and lanthanide (Ln = Eu or Yb/Er) nitrate, with the molar desired content of lanthanide needed in the nanoparticles ([Ln] = 0.1 M), was added dropwise to a freshly prepared orthovanadate aqueous solution ([V] = 0.1 M, pH = 12.5−13) of the same volume under vigorous stirring. During the nitrate addition, a milky precipitate appears corresponding to the formation of the solid phase YVO_4:Ln. Some drops of hydroxide sodium 1 M were added to maintain the pH above 9 during the addition. The solution was then left under stirring for 30 min and purified by dialysis against pure water until its conductivity lies below 100 $\mu S \cdot cm^{-1}$. The YVO_4 particles were then stabilized by adding a solution of poly(acrylic acid) PAA ($M_w \sim 1800\ g \cdot mol^{-1}$) which was diluted in ammonium hydroxide 28%, in order to obtain a final pH of 8.4. The molar ratio V:PAA was 1:0.05. The final solution was then sonified (with the 450 W Branson sonifier) for 5 min, leading to a homogeneous, slightly diffusing colloidal suspension.

Heat Treatment of Oxide Nanoparticles. The polymeric silica sol was prepared under acidic conditions by mixing TEOS ($Si(OC_2H_5)_4$), water (pH 1.25), and ethanol in the 1:5:3.8 molar ratio, and aged 1 h at 60 °C. In order to be able to dissolve more easily this silica matrix, a porous structure was prepared from a sol−gel silica gelation around self-organized micellar assemblies of a templating copolymer surfactant. The Pluronic PE6800 copolymer ($EO_{73}PO_{28}EO_{73}$), $M_w \sim 8080\ g \cdot mol^{-1}$, supplied by BASF Europe, was dissolved in ethanol at $40.4\ g \cdot L^{-1}$. The final solution was obtained by mixing the colloidal solution, the silica sol, and the PE6800 solution. Note that, for YVO_4:Eu particles, the basic character of the colloidal solution implies using concentrations of surfactant in the sol which do not systematically lead to an organized silica matrix (usual V:Si:PE6800 molar ratios are 1:5:0.05). The gel was dried at 90 °C for over 6 h, and the resulting powder was annealed under air at 1000 °C in two steps. A first annealing was realized at 500 °C with a speed 100 °C/h and a final stage of 1 h and the second at 1000 °C with a speed 100 °C/h and with two stages of 2 h at 500 °C and 10 min at 1000 °C. The first annealing is necessary for a complete removal of organic material (polymers PAA and PE6800). The final temperature of the second annealing was optimized in order to obtain the best crystallization of nanoparticles in an amorphous silica matrix.

Dispersion of Annealed Particles in Water. The silica powder containing oxide particles was thus dissolved by hydrofluoric acid 2% in excess during 3 h in the molar ratio of Si:HF 1:9. The hydrofluoric acid and the dissolved silica were then eliminated by two centrifugations at 14000*g*, the first for 1 min and the second for 10 min. The precipitates were diluted in pure water and some drops of hydroxide sodium to fix the pH at 10−11. The final solution was stabilized by the addition of PAA (V:PAA 1:0.05) and the sonification in a cold bath during 5 min.

Characterizations. Dynamic light scattering and ζ-potentials were obtained on a Malvern zetasizer. Nitrogen adsorption isotherms were recorded on a Micromeritics ASAP 2001 apparatus and analyzed from the BET model to deduce surface area values (see Figure S1 in Supporting Information). Electron microscopy experiments were made using a Philips CM30 microscope operating at 300 kV and a FEG-SEM Hitachi 4800. X-ray diffraction (XRD) was performed on powders using a Philips X-Pert diffractometer with Cu Kα radiation. The coherence length ς was deduced from the full width at half-maximum of the diffraction peaks using Scherrer's law. It approximately corresponds to the average size of particles only in the case of single-crystalline particles. Size-strain analysis of X-ray diagrams was conducted using the Williamson−Hall procedure (see Figure S2 in Supporting Information).[21] Luminescence spectra of YVO_4:Eu colloids were recorded on a commercial Hitachi F-4500 spectrofluorometer. The emission quantum yields of colloidal suspensions were determined by comparing their integrated emission intensity (from the $^5D_0$ level of Eu ions) with the emission from a Rhodamine 6G solution in ethanol having the same optical density (OD < 0.3) and excited at the same wavelength (280 nm).

Supporting Information Available: More characterizations of the mesoporous silica matrix including N_2 adsorption isotherms (Figure 1S) and of annealed nanoparticles including Williamson−Hall analysis of X-ray diffraction patterns (Figure 2S). This material is available free of charge *via* the Internet at http://pubs.acs.org.

REFERENCES AND NOTES

1. Pankhurst, Q. A.; Connolly, J.; Jones, S. K.; Dobson, J. Applications of Magnetic Nanoparticles in Biomedecine. *J. Phys. D: Appl. Phys.* **2003**, *36*, R167–R181.
2. Gupta, A. K.; Gupta, M. Applications of Magnetic Nanoparticles in Biomedecine. *Biomaterials* **2005**, *26*, 3995–4021.
3. Insin, N.; Tracy, J. B.; Lee, H.; Zimmer, J.-P.; Westervelt, R. M.; Bawendi, M. G. Incorporation of Iron Oxide Nanoparticles and Quantum Dots into Silica Microspheres. *ACS Nano* **2008**, *2*, 197–202.
4. Beaurepaire, E.; Sauviat, M.-P.; Giaume, D.; Lahlil, K.; Mercuri, A.; Casanova, D.; Huignard, A.; Martin, J.-L.; Gacoin, T.; Boilot, J.-P.; *et al.* Functionalized Fluorescent Oxide Nanoparticles: Artificial Toxins for Sodium Channel Targeting and Imaging at the Single-Molecule Level. *Nano Lett.* **2004**, *4*, 2079–2083.
5. Louis, C.; Bazzi, R.; Marquette, C. A.; Bridot, J.-L.; Roux, S.; Ledoux, G.; Mercier, B.; Blum, L.; Perriat, P.; Tillement, O. Nanosized Hybrid Particles with Double Luminescence for Biological Labeling. *Chem. Mater.* **2005**, *17*, 1673–1682.
6. Dosev, D.; Nichkova, M.; Liv, M. Z.; Guo, B.; Liv, G. Y.; Hammock, B. D.; Kennedy, I. M. Application of Luminescent Eu: Gd_2O_3 Nanoparticles to the Visualization

of Protein Micropatterns. *J. Biomed. Opt.* **2005**, *10*, 064006–064012.
7. Mills, A.; Le Hunte, S. An Overview of Semiconductor Photocatalysis. *J. Photochem. Photobiol.* **1997**, *108*, 1–35.
8. Minabe, T.; Tryk, D. A.; Sawunyama, P.; Kikuchi, Y.; Hashimoto, K.; Fujishima, A. TiO_2-Mediated Photodegradation of Liquid and Solid Organic Compounds. *J. Photochem. Photobiol. A* **2000**, *137*, 53–62.
9. Pruden, A. L.; Ollis, D. F. Photoassisted Heterogeneous Catalysis—The Degradation of Trichloroethylene in Water. *J. Catal.* **1983**, *82*, 404–417.
10. Deshpande, A.; Pinna, N.; Beato, P.; Antonietti, M.; Niederberger, M. Synthesis and Characterization of Stable and Crystalline $Ce_{1-x}Zr_xO_2$ Nanoparticle Sols. *Chem. Mater.* **2004**, *16*, 2599–2604.
11. O'Brien, S.; Brus, L.; Murray, C. B. Synthesis of Monodisperse Nanoparticles of Barium Titanate: Towards a Generalized Strategy of Oxide Nanoparticle Synthesis. *J. Am. Chem. Soc.* **2001**, *123*, 12085–12086.
12. Murray, C. B.; Kagan, C. R.; Bawendi, M. G. Synthesis and Characterization of Monodisperse Nanocrystals and Close-Packed Nanocrystal Assemblies. *Annu. Rev. Mater. Sci.* **2000**, *30*, 545–610.
13. Riwotzki, K.; Haase, M. Wet-Chemical Synthesis of Doped Colloidal Nanoparticles YVO_4:Ln (Ln = Eu, Sm, Dy). *J. Phys. Chem. B* **1998**, *102*, 10129–10135.
14. Meyssamy, H.; Riwotzki, K.; Kornowski, A.; Naused, S.; Haase, M. Wet Chemical Synthesis of Doped Colloidal Nanomaterials: Particles and Fibers of $LaPO_4$:Eu, $LaPO_4$:Ce, $LaPO_4$:Ce,Tb. *Adv. Mater.* **1999**, *11*, 840–844.
15. Buissette, V.; Giaume, D.; Gacoin, T.; Boilot, J.-P. Aqueous Routes To Lanthanide-Doped Oxide Nanophosphors. *J. Mater. Chem.* **2006**, *16*, 529–539.
16. Park, J. H.; Vescovo, E.; Kim, H.-J.; Kwon, C.; Ramesh, R.; Venkatesan, T. Magnetic Properties at Surface Boundary of a Half-Metallic Ferromagnet $La_{0.7}Sr_{0.3}MnO_3$. *Phys. Rev. Lett.* **1998**, *81*, 1953–1956.
17. Van Uitert, L. G.; Johnson, L. F. Energy Transfer between Rare-Earth Ions. *J. Chem. Phys.* **1966**, *44*, 3514–3522.
18. Poluektov, N. S.; Gava, S. A. Concentration Dependence of Lanthanide Luminescence in Yttrium Orthovanadate Phosphors. *Opt. Spectros. USSR* **1971**, *31*, 45–48.
19. Huignard, A.; Gacoin, T.; Boilot, J.-P. Synthesis and Luminescence Properties of Colloidal YVO_4:Eu Phosphors. *Chem. Mater.* **2000**, *12*, 1090–1094.
20. Puzenat, E.; Pichat, P. Studying TiO_2 Coatings on Silica-Covered Glass by O^{2-} Photosorption Measurements and FTIR-ATR Spectrometry—Correlation with the Self-Cleaning Efficacity. *J. Photochem. Photobiol. A* **2003**, *160*, 127–133.
21. Besson, S.; Ricolleau, C.; Gacoin, T.; Jacquiod, C.; Boilot, J.-P. Highly Ordered Orthorhombic Mesoporous Silica Films. *Microporous Mesoporous Mater.* **2003**, *60*, 43–49.
22. Jenkins, R.; Snyder, R. L. *X-Ray Powder Diffractometry*; Wiley-Interscience: New York, 1996; pp 89−91.
23. Langford, J. I.; Louër, D. Powder Diffraction. *Rep. Prog. Phys.* **1996**, *59*, 131–234.
24. Iller, R. K. *The Chemistry of Silica*; Wiley: New York, 1979.
25. Daniels, M. W.; Sefcik, J.; Francis, L. F.; McCormick, A. V. Reaction of a Trifunctional Silane Coupling Agent in the Presence of Colloidal Silica Sols in Polar Media. *J. Colloid Interface Sci.* **1999**, *219*, 351–356.
26. Huignard, A.; Buissette, V.; Franville, A. C.; Gacoin, T.; Boilot, J.-P. Emission Processes in YVO_4:Eu Nanoparticles. *J. Phys. Chem. B* **2003**, *107*, 6754–6759.
27. Ropp, R. C. Spectra of Some Rare Earth Vanadates. *J. Electrochem. Soc.* **1968**, *115*, 940–945.
28. Asahi, R.; Morikawa, T.; Ohwaki, T.; Aoki, K.; Taga, Y. Visible-Light Photocatalysis in Nitrogen-Doped Titanium Oxides. *Science* **2001**, *293*, 269–272.
29. Livraghi, S.; Paganini, M. C.; Giarnello, E.; Selloni, A.; Di Valentin, C.; Pacchioni, G. Origin of Photoactivity of Nitrogen-Doped Titanium Dioxide under Visible Light. *J. Am. Chem. Soc.* **2006**, *128*, 15666–15671.
30. Allain, E.; Besson, S.; Durand, C.; Moreau, M.; Gacoin, T.; Boilot, J.-P. Transparent Mesoporous Nanocomposite Films for Self-Cleaning Applications. *Adv. Funct. Mater.* **2007**, *17*, 549–554.
31. Mills, A.; Davies, R. H.; Worsley, D. Water-Purification by Semiconductor Photocatalysis. *Chem. Soc. Rev.* **1993**, *22*, 417–425.
32. Hebbink, G. A.; Stouwdam, J. W.; Reinhoudt, D. N.; Van Veggel, F. C. J. M. Lanthanide Doped Nanoparticles that Emit in the Near-Infrared. *Adv. Mater.* **2002**, *14*, 1147–1150.
33. Heer, S.; Lehmann, O.; Haase, M.; Güdel, H. U. Blue, Green, and Red Upconversion Emission from Lanthanide-Doped $LuPO_4$ and $YbPO_4$ Nanocrystals in a Transparent Colloidal Solution. *Angew. Chem., Int. Ed.* **2003**, *42*, 3179–3182.